Eight-band k.p calculations of the composition contrast effect on the linear polarization properties of columnar quantum dots

Please check the document version of this publication:

• A submitted manuscript is the version of the article upon submission and before peer-review. There can be important differences between the submitted version and the official published version of record. People interested in the research are advised to contact the author for the final version of the publication, or visit the DOI to the publisher's website.
• The final author version and the galley proof are versions of the publication after peer review.
• The final published version features the final layout of the paper including the volume, issue and page numbers.

Link to publication

Eight-band k·p calculations of the composition contrast effect on the linear polarization properties of columnar quantum dots

Janusz Andrzejewski,[1,a)] Grzegorz Sęk,[1] Eoin O'Reilly,[2] Andrea Fiore,[3] and Jan Misiewicz[1]

[1]*Institute of Physics, Wroclaw University of Technology, Wybrzeze Wyspianskiego 27, 50-370 Wroclaw, Poland*
[2]*Department of Physics, Tyndall National Institute, University College Cork, Lee Maltings, Cork, Ireland*
[3]*COBRA Research Institute, Eindhoven University of Technology, P.O. Box 513, 5600 MB Eindhoven, The Netherlands*

We present eight-band $\mathbf{k} \cdot \mathbf{p}$ calculations of the electronic and polarization properties of columnar $In_zGa_{1-z}As$ quantum dots (CQD) with high aspect ratio embedded in an $In_xGa_{1-x}As/GaAs$ quantum well. Our model accounts for the linear strain effects, linear piezoelectricity, and spin-orbit interaction. We calculate the relative intensities of transverse-magnetic (TM) and transverse-electric (TE) linear polarized light emitted from the edge of the semiconductor wafer as a function of the two main factors affecting the heavy hole—light hole valence band mixing and hence, the polarization dependent selection rules for the optical transitions, namely, (i) the composition contrast z/x between the dot material and the surrounding well and (ii) the dot aspect ratio. The numerical results show that the former is the main driving parameter for tuning the polarization properties. This is explained by analyzing the biaxial strain in the CQD, based on which it is possible to predict the TM to TE intensity ratio. The conclusions are supported by analytical considerations of the strain in the dots. Finally, we present the compositional and geometrical conditions to achieve polarization independent emission from InGaAs/GaAs CQDs. © *2010 American Institute of Physics*. [doi:10.1063/1.3346552]

I. INTRODUCTION

The effects of strain on the electronic band structure have been reported for a variety of quantum dot (QD) shapes, such as flat cylinders,[1] pyramids,[2] lenses,[3] and cones.[4] There exist also examinations of the importance of the height-to-base ratio for pyramid,[5] truncated-pyramid,[6] and other realistic dot shapes.[7] A common conclusion which is usually drawn is that the dot volume has the primary effect on the electronic structure. Even more, the essential features of the confinement potential are determined mainly by one geometric parameter, i.e., the aspect ratio, with simultaneous insensitivity to other details of the QD shape.[7] One parameter of interest is the orientation of the dipole moment, which determines the polarization of the emitted light. In self-assembled QDs, optical transitions between the conduction and valence band states for in-plane light propagation are strong in the transverse-electric (TE) mode of the light polarization (polarization vector in the structure plane), with rather weak transverse-magnetic (TM) component (polarization vector along the growth direction). This has been explained by computer simulations using a multiband Hamiltonian to be a direct consequence of the "flat" dot geometry and of the predominantly heavy-hole (HH) character of the highest valence band states.[8]

However, control of the polarization of the emitted light can be highly beneficial in some optoelectronic applications.

It has been recently demonstrated experimentally that semiconductor QDs with large height to base length ratio are able to emit polarization independent light from the edge of the wafer. This is of significant potential benefit for semiconductor optical amplifiers, allowing polarization-independent gain from a dotlike emitter.[9–14] Such "columnar" QDs (CQDs) with large aspect ratio can, for example, be obtained by cycled submonolayer deposition,[15] and are thus promising candidates for amplifier applications. On the other hand, the analysis of the physics responsible for the observed polarization properties of such nano-objects is still rather limited and has considered only the influence of the dot geometry within quite a narrow aspect ratio range of 1–1.8 (height to the base length) for pure InAs dots on GaAs.[16] In particular, the role of the material surrounding the CQD on the strain and thus on the polarization properties has not been considered. Indeed, due to the growth technique employed, CQDs are laterally immersed in a material with a composition intermediate between that of the matrix and of the CQD.[17] In fact, in a common implementation CQDs are formed by depositing a short-period InAs/GaAs superlattice on a seeding InAs self-assembled QD layer. Each seeding dot causes a strain field, which drives the preferential growth of InAs on top of the QD, resulting in the formation of In-rich columns immersed in an InGaAs layer.[18,19] A very similar kind of growth can take place in other material systems, including, e.g., growth on InP substrates.[9,13] The composition of the two-dimensional (2D) surrounding layer (which we refer to as the "immersion layer") can be at least partly controlled by the growth parameters.[19] This is necessary when growing QDs

a)Electronic mail: janusz.andrzejewski@pwr.wroc.pl.

with extremely high aspect ratios, for which values exceeding 10 have been demonstrated.[19] Because the existence of this immersion layer changes not only the carrier confinement directly but also the strain distribution, it affects significantly the valence band mixing effects and hence the polarization dependent selection rules. In this work, we use eight-band $\mathbf{k \cdot p}$ numerical calculations, supported also by analytical considerations of the strain, to investigate the effects of the immersion layer and of the CQD aspect ratio on the polarization properties of CQD structures. Our results show clearly that the compositional contrast between this layer and the dot is considerably more important than the dot geometry for the range of high dot aspect ratios considered here (from 3 to 6). We present details of the numerical methods used in the Sec. II. Our analytical and numerical results are presented in Sec. III. Finally we summarize our conclusions in Sec. IV.

II. NUMERICAL MODEL

For the calculations of the electronic states and optical transitions in CQDs we have developed a three-dimensional (3D) strain-dependent eight-band $\mathbf{k \cdot p}$ model. The model is implemented and all physical equations are numerically solved using the finite difference method. The model includes strain fields, piezoelectric effects, and the spin-orbit interaction. This type of model has previously been applied successfully to the analysis of various types of zinc-blende material QDs.[8,16,20,21]

A. Calculation of the strain

The linear strain field has been calculated using continuum mechanical elastic theory. The detailed description of such calculations is given, for instance, in Refs. 22 and 23 or Refs. 2 and 8. The elastic energy U comes from the dependence of the intrinsic lattice parameter on the alloy composition in the system and is given by[24]

$$U = \frac{1}{2} \int_V \sum_{i,j,k,l} C_{ijkl}(\vec{r}) \varepsilon_{ij}(\vec{r}) \varepsilon_{kl}(\vec{r}) d\vec{r}, \qquad (1)$$

where $C_{ijkl}(\vec{r})$ is the elastic constants tensor, $\varepsilon_{ij}(\vec{r})$ is the elastic strain tensor, V is the total volume of the system, and i, j, k, l run over the spatial coordinates x, y, and z. To account for the lattice mismatch, the strain tensor $\varepsilon_{ij}(\vec{r})$ is represented as

$$\varepsilon_{ij}(\vec{r}) = \varepsilon^u_{ij}(\vec{r}) - \varepsilon^o_{ij}(\vec{r}), \qquad (2)$$

where $\varepsilon^o_{ij}(\vec{r})$ is the local intrinsic strain induced by the changes in the lattice constant. For a material with a cubic symmetry $\varepsilon^o_{ij}(\vec{r})$ is given by

$$\varepsilon^o_{ij}(\vec{r}) = \frac{a(\vec{r}) - a_{\mathrm{matrix}}}{a_{\mathrm{matrix}}} \delta_{ij}, \qquad (3)$$

where $a(\vec{r})$ equals the lattice constant at position $\vec{r}$ and a_{matrix} is the lattice constant of the matrix in which the QD is em-

bedded. The six components of the strain tensor $\hat{\varepsilon}$ are not independent quantities but are determined from the three components of the displacement vectors $\vec{u}$ as follows:

$$\varepsilon^u_{ij}(\vec{r}) = \frac{1}{2} \left(\frac{\partial u_i}{\partial x_j} + \frac{\partial u_j}{\partial x_i} \right). \qquad (4)$$

The strain field can be obtained by inserting Eqs. (2)–(4) into Eq. (1), as is done, for example, in Refs. 22 and 23, U is then minimized with respect to $\vec{u}$ throughout the entire solution space and the displacement vector field can be obtained. By using Eq. (4), the local strain tensor can be calculated and then the physical strain can be obtained by using Eq. (2).[23]

Numerical solution of Eq. (1) requires discretization of the structure. The displacements u_i are discretized at the mesh nodes, with their first derivatives represented by finite differences. As suggested in[23] central differences are avoided, so the first derivative is averaged over the eight permutations of the forward and backward differences.

The integration of Eq. (1) is performed in a rectangular parallelepiped (numerical box) large enough to completely enclose the QD or dots so that the faces of the box should have negligible influence on the strain field. Furthermore, at the faces of the numerical box the appropriate boundary condition have to be applied.[24] A fixed boundary condition is used at the base of the box while free-standing boundary conditions are implemented at the other faces of the box. The entire parallelepiped is divided into a rectangular mesh, with the principal axes along the [100], [010], and [001] directions.

Minimization of the elastic energy reduces Eq. (1) to a system of linear equations[25]

$$\frac{dU}{du_x(ijk)} = \frac{dU}{du_y(ijk)} = \frac{dU}{du_z(ijk)} = 0, \qquad (5)$$

in which $u_\xi(ijk)$ represents the value of the $\xi = (x, y, z)$ component of the displacement vector at the ijk node. Each node is coupled with 26 neighboring nodes,[23] which when multiplied by the three components of the displacement vectors gives a total of 81 nonzero coefficients in each equation. The system of linear equations is efficiently solved by the preconditioned conjugate gradient method.

B. Piezoelectricity

Piezoelectricity arises when the effects of strain in a crystal lacking a center of symmetry leads to the generation of electric polarization. The zinc-blende structure is one of the simplest lattice examples in which the strength of the resulting polarization in the linear case is described by one parameter e_{14}. The second-order piezoelectric effect[26] is only included in the effective values of the experimental linear piezoelectric coefficients we used in our calculations, i.e., they mimic a combined contribution of both the first and second-order piezoelectric effects. The polarization $\vec{P}$ is related to the strain tensor field by

$$\vec{P}(\vec{r}) = 2e_{14}(\vec{r})[\varepsilon_{yz}(\vec{r}), \varepsilon_{xz}(\vec{r}), \varepsilon_{xy}(\vec{r})]. \qquad (6)$$

Piezoelectric charges, ρ_{piezo} arise from the polarization

$$\rho_{\text{piezo}}(\vec{r}) = - \nabla \cdot \vec{P}(\vec{r}). \tag{7}$$

The resulting piezoelectric potential V_P is obtained by solving Poisson's equation

$$\rho_{\text{piezo}}(\vec{r}) = \varepsilon_0 \nabla \cdot [\varepsilon_s(\vec{r}) \nabla V_P(\vec{r})], \tag{8}$$

where $\varepsilon_s(\vec{r})$ is the static dielectric constant. The right hand side of Eq. (8) is represented by the direct finite difference,[27] where the material dependence of the dielectric constant is also taken into account. In the one-dimensional case (for instance along the x-axis, at the point $x = x_0 + ih$, where h is the mesh length) the direct finite difference for the second derivative is given by

$$\frac{d}{dx} \varepsilon \frac{d}{dx} V \bigg|_{x=x_0+ih} = \frac{1}{2h^2} [(\varepsilon_i + \varepsilon_{i-1}) V_{i-1} - (\varepsilon_{i-1} + 2\varepsilon_i + \varepsilon_{i+1}) V_i + (\varepsilon_i + \varepsilon_{i+1}) V_{i+1}], \tag{9}$$

where $\varepsilon_i = \varepsilon(x_0 + ih)$ and $V_i = V(x_0 + ih)$. The resulting linear set of equations is solved by the conjugate gradient method.

C. Calculation of energy levels

Calculation of the energy levels in the CQDs is performed by using an eight-band $\mathbf{k} \cdot \mathbf{p}$ model, as described by Bahder.[28] This is a multiband effective mass theory, which exactly includes the spin down and spin up Bloch waves from the lowest conduction band and the spin up and spin down functions from each of the three degenerate highest p-like valence bands (set A). The other (remote) bands are included via perturbation theory (set B). In the framework of the envelope function approximation, the states of the system $\Psi(\vec{r})$ are described as[29]

$$\Psi(\vec{r}) = \sum_{N}^{set\ A} \phi_N(\vec{r}) u_{N\vec{k}_0}(\vec{r}) = \sum_{M} \sum_{j=1}^{2} \phi_M^j(\vec{r}) u_{M\vec{k}_0}^j(\vec{r}), \tag{10}$$

where $u_{M\vec{k}_0}^j(\vec{r})$ are bulk band edge Bloch functions (central cell) at the $\vec{k}_0$ point in the Brillouin zone and $\phi_M^j(\vec{r})$ are envelope functions. The most common choice for the $\vec{k}_0$ point is the Γ point ($\vec{k}_0 = 0$) and all the parameters which enter into the theory are taken at the Γ point. The central cell

Bloch functions are expressed as[28]

$$u_{\text{EL}}^1 = |s\rangle \chi_{\downarrow}. \tag{11a}$$

$$u_{\text{EL}}^2 = |s\rangle \chi_{\uparrow}. \tag{11b}$$

$$u_{\text{LH}}^1 = \frac{-i}{\sqrt{6}} (|x\rangle + i|y\rangle) \chi_{\downarrow} + i \sqrt{\frac{2}{3}} |z\rangle \chi_{\uparrow}. \tag{11c}$$

$$u_{\text{HH}}^1 = \frac{i}{\sqrt{2}} (|x\rangle + i|y\rangle) \chi_{\uparrow}. \tag{11d}$$

$$u_{\text{HH}}^2 = \frac{-i}{\sqrt{2}} (|x\rangle - i|y\rangle) \chi_{\downarrow}. \tag{11e}$$

$$u_{\text{LH}}^2 = \frac{i}{\sqrt{6}} (|x\rangle - i|y\rangle) \chi_{\uparrow} + i \sqrt{\frac{2}{3}} |z\rangle \chi_{\downarrow}. \tag{11f}$$

$$u_{\text{SO}}^1 = \frac{-i}{\sqrt{3}} (|x\rangle - i|y\rangle) \chi_{\uparrow} + \frac{i}{\sqrt{3}} |z\rangle \chi_{\downarrow}. \tag{11g}$$

$$u_{\text{SO}}^2 = \frac{-i}{\sqrt{3}} (|x\rangle + i|y\rangle) \chi_{\downarrow} - \frac{i}{\sqrt{3}} |z\rangle \chi_{\uparrow}. \tag{11h}$$

In the above equations, $|s\rangle$ is the s-like conduction band function, and $|x\rangle$, $|y\rangle$, and $|z\rangle$ are p-like valence band functions, $\chi_{\uparrow}$ and $\chi_{\downarrow}$ are the eigenspinors of the Pauli spin matrix σ_z and M runs over EL, LH, HH, SO for electron, light hole, heavy hole, and spin-orbit, respectively. It should be noted that the Bloch states are doubly degenerate, due to time-reversal symmetry. The time-reversal operator for our basis functions is given by[28]

$$T = \begin{bmatrix} J & 0 & 0 & 0 \\ 0 & 0 & J & 0 \\ 0 & J & 0 & 0 \\ 0 & 0 & 0 & J \end{bmatrix} \hat{K}, \tag{12a}$$

where

$$J = \begin{bmatrix} 0 & -1 \\ 1 & 0 \end{bmatrix} \text{ and } 0 = \begin{bmatrix} 0 & 0 \\ 0 & 0 \end{bmatrix}, \tag{12b}$$

and $\hat{K}$ denotes complex conjugation.

As a result of this approximation the Schrödinger equation is converted into a set of eight coupled differential equations for the envelope functions, where the Hamiltonian H has the form

$$H = \begin{bmatrix} A & 0 & V^* & 0 & \sqrt{3}V & -\sqrt{2}U & -U & \sqrt{2}V^* \\ 0 & A & -\sqrt{2}U & \sqrt{3}V^* & 0 & -V & \sqrt{2}V & U \\ V & -\sqrt{2}U & -P+Q & -S^* & R & 0 & \sqrt{\tfrac{3}{2}}S & -\sqrt{2}Q \\ 0 & -\sqrt{3}V & -S & -P-Q & 0 & R & -\sqrt{2}R & \tfrac{1}{\sqrt{2}}S \\ \sqrt{3}V^* & 0 & R^* & 0 & -P-Q & S^* & \tfrac{1}{\sqrt{2}}S^* & \sqrt{2}R^* \\ -\sqrt{2}U & -V^* & 0 & R^* & S & -P+Q & \sqrt{2}Q & \sqrt{\tfrac{3}{2}}S^* \\ -U & \sqrt{2}V^* & \sqrt{\tfrac{3}{2}}S^* & -\sqrt{2}R^* & \tfrac{1}{\sqrt{2}}S & \sqrt{2}Q & -P-\Delta & 0 \\ \sqrt{2}V & U & -\sqrt{2}Q & \tfrac{1}{\sqrt{2}}S^* & \sqrt{2}R & \sqrt{\tfrac{3}{2}}S & 0 & -P-\Delta \end{bmatrix}, \tag{13}$$

where

$$A = E_C + \gamma_C(k_x^2 + k_y^2 + k_z^2) + a_C(\varepsilon_{xx} + \varepsilon_{yy} + \varepsilon_{zz}). \tag{14a}$$

$$U = \frac{1}{\sqrt{3}}P_0 k_z + \frac{1}{\sqrt{3}}P_0 \sum_j \varepsilon_{zj} k_j. \tag{14b}$$

$$V = \frac{1}{\sqrt{6}}P_0(k_x - ik_y) + \frac{1}{\sqrt{6}}P_0 \sum_j (\varepsilon_{xj} - i\varepsilon_{yj})k_j. \tag{14c}$$

$$P = -E_V + \frac{1}{2}\gamma_1 \frac{\hbar^2}{m_0}(k_x^2 + k_y^2 + k_z^2) + a_V(\varepsilon_{xx} + \varepsilon_{yy} + \varepsilon_{zz}). \tag{14d}$$

$$Q = \frac{1}{2}\gamma_2 \frac{\hbar^2}{m_0}(k_x^2 + k_y^2 - 2k_z^2) + b_V\left[\varepsilon_{zz} - \frac{1}{2}(\varepsilon_{xx} + \varepsilon_{yy})\right]. \tag{14e}$$

$$R = -\frac{\sqrt{3}}{2}\frac{\hbar^2}{m_0}[\gamma_2(k_x^2 - k_y^2) - 2i\gamma_3 k_x k_y] + \frac{\sqrt{3}}{2}b_V(\varepsilon_{xx} - \varepsilon_{yy}) - id_V\varepsilon_{xy}. \tag{14f}$$

$$S = \sqrt{3}\gamma_3 \frac{\hbar^2}{m_0}k_z(k_x - ik_y) - d_V(\varepsilon_{xz} - i\varepsilon_{yz}). \tag{14g}$$

In Eqs. (13) and (14), E_C and E_V are the unstrained positions of the conduction and valence band energies, respectively, $E_g = E_C - E_V$ is the energy band gap, Δ is the spin-orbit splitting energy, and P_0 is the $\mathbf{k} \cdot \mathbf{p}$ matrix element describing the conduction-valence band coupling. The constants γ_1, γ_2, and γ_3 are the modified Luttinger parameters and are related[30] to the original Luttinger parameters γ_1^L, γ_2^L, and γ_3^L, by

$$\gamma_1 = \gamma_1^L - \frac{E_P}{3E_g}, \tag{15a}$$

$$\gamma_2 = \gamma_2^L - \frac{E_P}{6E_g}, \tag{15b}$$

$$\gamma_3 = \gamma_3^L - \frac{E_P}{6E_g}, \tag{15c}$$

where the optical matrix element E_P is given by

$$E_P = \frac{2m_0}{\hbar^2}P_0^2. \tag{15d}$$

a_C is the conduction band hydrostatic deformation potential, a_V is the valence band hydrostatic deformation potential (where the energy gap deformation potential $a_g = a_C + a_V$), b_V is the valence band axial deformation potential associated with strain along the [100] crystallographic direction, and d_V is the shear deformation potential, for strain along the [111] direction. In the Hamiltonian of Eq. (13) the parameters B (connected with the inversion symmetry) and b' (connected with the coupling of the conduction band with shear deformations) are neglected.[20]

As this theory was originally developed for strained zinc-blende crystals, the equations must be augmented for heterostructures by boundary conditions, which describe how the envelope functions are to be joined at the boundaries of adjacent regions.[31–37] For QDs, the operator of Eq. (13) is converted into a differential operator via the replacement

$$k_\mu \to \frac{1}{i}\frac{\partial}{\partial x_\mu}, \tag{16}$$

and all of the parameters are considered as functions of position. The partial derivatives for a position dependent $\tilde{P}$ and $\tilde{Q}$ are then symmetrized according to the scheme[38]

$$\tilde{P}\frac{\partial}{\partial x_\mu} \to \frac{1}{2}\left[\tilde{P}\frac{\partial}{\partial x_\mu} + \frac{\partial}{\partial x_\mu}\tilde{P}\right], \tag{17a}$$

$$\tilde{Q}\frac{\partial}{\partial x_\mu}\frac{\partial}{\partial x_\nu} \rightarrow \frac{1}{2}\left[\frac{\partial}{\partial x_\mu}\tilde{Q}\frac{\partial}{\partial x_\nu} + \frac{\partial}{\partial x_\nu}\tilde{Q}\frac{\partial}{\partial x_\mu}\right], \quad (17b)$$

where

$$\tilde{P} = P_0, \varepsilon_{zx}, \varepsilon_{zy}, \varepsilon_{zz}, \quad (17c)$$

$$\tilde{Q} = \gamma_C, \gamma_1, \gamma_2, \gamma_3. \quad (17d)$$

For one dimension along the x-axis at the point $x_i = x_0 + ih$, the harmonic finite difference method[27] was used to define the second derivative in Eq. (17b)

$$\frac{d}{dx}\tilde{Q}\frac{d}{dx}\psi = \frac{1}{2h^2}\left[\left(\frac{1}{m_i}+\frac{1}{m_{i-1}}\right)\psi_{i-1} - \left(\frac{1}{m_{i-1}}+\frac{2}{m_i}\right.\right.$$
$$\left.\left. +\frac{1}{m_{i+1}}\right)\psi_i + \left(\frac{1}{m_i}+\frac{1}{m_{i+1}}\right)\psi_{i+1}\right], \quad (18)$$

and for the first derivatives of Eq. (17a) the second-order upwind scheme[39] was used

$$\frac{d}{dx}\tilde{P}\psi$$
$$= \begin{cases} \frac{1}{2h^2}(3\tilde{P}_i\psi_i - 4\tilde{P}_{i-1}\psi_{i-1} + \tilde{P}_{i-2}\psi_{i-2}) & for \quad \tilde{P}>0 \\ \frac{1}{2h^2}(-\tilde{P}_{i+2}\psi_{i+2} + 4\tilde{P}_{i+1}\psi_{i+1} - 3\tilde{P}_i\psi_i) & for \quad \tilde{P}<0 \end{cases}, \quad (19)$$

where $\psi_i = \psi(x_i)$, $\tilde{P}_i = \tilde{P}(x_i)$, and $\tilde{Q}_i = \tilde{Q}(x_i)$.

After discretization of the eight-band **k·p** Hamiltonian using the above prescription, the resulting secular equation is solved using the Jacobi–Davidson[40] algorithm.

Because of numerical instabilities with $\gamma_C < 0$,[41] we rescale E_P to a value that keeps $\gamma_C \equiv 1$. The fitting equation for the optical matrix parameter

$$\gamma_C(\vec{r}) = \frac{1}{m_C(\vec{r}) - E_P(\vec{r})}\frac{E_g(\vec{r}) + \frac{2}{3}\Delta(\vec{r})}{E_g(\vec{r})[E_g(\vec{r}) + \Delta(\vec{r})]} \equiv 1, \quad (20)$$

then gives

$$E_P(\vec{r}) = \left(\frac{1}{m_c(\vec{r})} - 1\right)\frac{E_g(\vec{r})[E_g(\vec{r}) + \Delta(\vec{r})]}{E_g(\vec{r}) + \frac{2}{3}\Delta(\vec{r})}. \quad (21)$$

D. Calculation of polarization properties

In order to calculate the TE-mode and TM-mode transition intensities in the CQDs, we first calculate the oscillator strength f_S for the electron-hole transition between the two states, ψ^i and ψ^f, with energies E_i and E_f, respectively, as[29]

$$f_S = \frac{2}{m_0}\frac{|\langle\psi^f|\vec{e}\cdot\vec{p}|\psi^i\rangle|^2}{E_f - E_i}, \quad (22)$$

where $\vec{e}$ is the direction unit vector for the electric field (polarization) of the light.

The momentum matrix element is calculated as[42]

$$\langle\psi^f|\vec{e}\cdot\vec{p}|\psi^i\rangle = \sum_{N,N'}^{set\,A}\frac{m_0}{\hbar}\vec{e}\cdot\langle\phi_N^f|\frac{\partial H_{N,N'}(\vec{k})}{\partial\vec{k}}|\phi_{N'}^i\rangle, \quad (23)$$

where $\psi^l = [\phi_{EL1}^l, \phi_{EL2}^l, \phi_{LH1}^l, \phi_{HH1}^l, \phi_{HH2}^l, \phi_{LH2}^l, \phi_{SO1}^l, \phi_{SO2}^l]$ is the vector of envelope functions for state l, and l runs over the initial (i) and final (f) states.

For the QD the operator $\vec{e}\cdot\vec{p}$ can be written in the form[42]

$$\vec{e}\cdot\vec{p} = \frac{m_0}{2\hbar}\vec{e}\cdot\left\{2\vec{P} + \left[Q\left(\frac{1}{i}\frac{\vec{d}}{dz}\right) + \left(\frac{1}{i}\frac{\vec{d}}{dz}\right)^*Q\right]\right.$$
$$+ \left[R\left(\frac{1}{i}\frac{\vec{d}}{dx}\right) + \left(\frac{1}{i}\frac{\vec{d}}{dx}\right)^*R\right] + \left[S\left(\frac{1}{i}\frac{\vec{d}}{dy}\right)\right.$$
$$\left.\left. + \left(\frac{1}{i}\frac{\vec{d}}{dy}\right)^*S\right]\right\}, \quad (24)$$

where the arrows indicate the direction in which the derivatives should be taken. It should be emphasized that this equation is valid for both intraband and interband transitions. The matrices for P, Q, R, and S could be calculated using the Hamiltonian of Eq. (13). It should be noted that for interband transitions, the main contribution to the momentum matrix element comes from the first term in Eq. (24). The first term could be written down as $\sum_{N,N'}^{set\,A}P_{NN'}\langle\phi_N^f|\phi_{N'}^i\rangle$. It is a sum of the overlapping of the fth final envelope function with the ith initial envelope function, with the weights given by the elements of the matrix $P_{NN'}$, where N and N' are the first (EL1) and second (EL2) electron, first (LH1) and second (LH2) light hole, first (HH1) and second (HH2) heavy hole, first (SO1) and second (SO2) spin orbit components of the final and initial total wave functions, respectively. The second, third, and fourth term have a similar form to the first one but the overlap is taken between the envelope function and the derivative of the envelope function.

For degenerate states a and b which satisfy Eq. (12a), $|\psi^{a1}\rangle = T|\psi^{a2}\rangle$ and $|\psi^{b1}\rangle = T|\psi^{b2}\rangle$ the momentum matrix elements $|\vec{e}\cdot\vec{p}_{ab}|$ for nonexcitonic transitions are obtained by incoherent averaging[8]

$$|\vec{e}\cdot\vec{p}_{ab}| = \frac{1}{4}(|\vec{e}\cdot\vec{p}_{a1b1}| + |\vec{e}\cdot\vec{p}_{a1b2}| + |\vec{e}\cdot\vec{p}_{a2b1}|$$
$$+ |\vec{e}\cdot\vec{p}_{a2b2}|). \quad (25)$$

All corrections due to excitonic effects are neglected in our calculations, and we assume a Gaussian broadening of each transition peak at energy $E_f - E_i$

$$I^k(E_t) = \sum_{i,f}\frac{|e\cdot p_{fi}|}{\sigma\sqrt{2}}\exp\left\{-\frac{[E_t - (E_f - E_i)]^2}{2\sigma^2}\right\}, \quad (26)$$

where σ (the standard deviation) is applied in order to simulate the experimental spectra and to allow for more direct comparison to the published experimental data on ensembles of dots, which are always affected by inhomogeneities in the dot properties.

III. RESULTS AND DISCUSSION

A. Analytical considerations

We consider a columnar $In_{x+y}Ga_{1-x-y}As$ dot embedded in an $In_xGa_{1-x}As$ quantum well (QW) (which plays the role of the 2D surrounding layer, i.e., an immersion layer) between GaAs barriers, with dot composition z then given by $z=x+y$. In linear elastic theory, the strain distribution can be treated as the sum of the strain due to a $In_xGa_{1-x}As$ QW plus the strain distribution due to an $In_yGa_{1-y}As$ CQD embedded in pure GaAs material. If we assume isotropic elastic constants, the strain distribution in the cuboid of height h and base area $d \times d$ can be calculated analytically.[43]

We estimate that the minimum requirement for a polarization insensitive QD is that the bulk HH and LH band edges are degenerate in the center of the QD. In practice, it is rather required for several reasons that the bulk LH band edge is the highest valence state at the center of the CQD. The larger HH mass in the growth (z) direction gives a smaller contribution to the total HH confinement energy than that due to the smaller LH mass in the z direction. The strain distribution varies through the CQD, with the LH band edge reaching its highest energy at the center of the CQD. When moving toward the top or bottom of the dot, the LH band edge will shift down in energy while the HH band edge shifts upwards in energy. There are two factors which affect the lateral contribution to the confinement energy, one of which pushes the LH down and the other of which pushes the LH up in energy. First, the larger lateral barrier for LHs, due to the compressive strain in the QW, pushes the LH down. On the other hand, the HH has a slightly lower in-plane mass than the LH, so this will tend to increase the lateral contribution to the HH confinement energy compared to the lateral contribution to the LH energy.

The HH and LH bulk edge energies are given in a strained structure as

$$E_{LH} = E_V + b\varepsilon_{ax}(z),$$ (27a)

$$E_{HH} = E_V - b\varepsilon_{ax}(z),$$ (27b)

where $E_V(z)$ is the mean energy of the HH and LH valence band maximum states and $\varepsilon_{ax}(z)$ is the axial strain component at z, with

$$\varepsilon_{ax}(z) = \varepsilon_{zz}(z) - \frac{1}{2}[\varepsilon_{xx}(z) + \varepsilon_{yy}(z)],$$ (28)

and where $\varepsilon_{ii}(z)$ is the ith component of the axial strain tensor. We, therefore, require as a minimum for degenerate HH and LH character that the total axial strain is zero at the center of the dot.

We have for a strained $In_xGa_{1-x}As$ QW on a GaAs substrate that

$$\varepsilon_{xx} = \varepsilon_{yy} = x\varepsilon_0,$$ (29a)

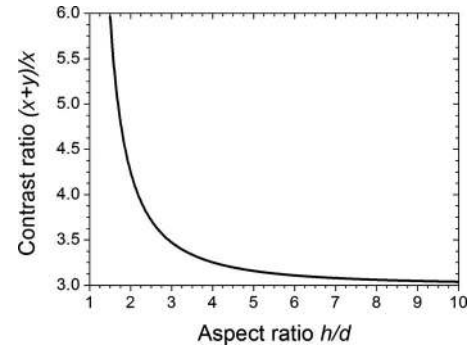$$\varepsilon_{zz} = -\frac{2\sigma}{1-\sigma}x\varepsilon_0,$$ (29b)

FIG. 1. Analytical calculation of contrast ratio of In composition $z=x+y$ in a CQD to In composition x in QW required in order to achieve zero net axial strain in center of dot as a function of ratio of dot height h to dot base length d.

$$\varepsilon_{ax} = -\frac{1+\sigma}{1-\sigma}x\varepsilon_0,$$ (29c)

Where ε_0 is the fractional difference in lattice constant between InAs and GaAs and σ is Poisson's ratio.

For zero net axial strain at the center of the CQD it is required that the axial strain there due to the $In_yGa_{1-y}As$ CQD is equal and opposite to that due to the strained $In_xGa_{1-x}As$ QW.

Assuming isotropic elastic constants, the axial strain can be calculated at the center of the cuboid QD, following the analysis in Ref. 43. It can be shown for a lattice mismatch strain ε_0 that

$$\varepsilon_{xx} = \varepsilon_0 - \frac{2\varepsilon_0(1+\sigma)}{\pi(1-\sigma)}\tan^{-1}\left(\frac{h}{\sqrt{2d^2+h^2}}\right).$$ (30a)

$$\varepsilon_{zz} = -\frac{2\varepsilon_0\sigma}{1-\sigma} + \frac{4\varepsilon_0(1+\sigma)}{\pi(1-\sigma)}\tan^{-1}\left(\frac{h}{\sqrt{2d^2+h^2}}\right).$$ (30b)

$$\varepsilon_{ax} = -\frac{\varepsilon_0(1+\sigma)}{\pi(1-\sigma)}\left[1 - \frac{6}{\pi}\tan^{-1}\left(\frac{h}{\sqrt{2d^2+h^2}}\right)\right].$$ (30c)

Comparing Eqs. (29c) and (30c), it can be seen that with an infinitely high dot (i.e., a wire) we get zero net strain at the center of the dot and degenerate LH and HH band edges when $y=2x$. This sets the first, lower limit on the difference in composition required between the dot and surrounding QW in order to achieve polarization insensitivity.

For a dot of finite height the net axial strain is zero ($\varepsilon_{ax}=0$) at the center of the dot when

$$-\frac{\varepsilon_0(1+\sigma)}{\pi(1-\sigma)}x - \frac{\varepsilon_0(1+\sigma)}{\pi(1-\sigma)}\left[1 - \frac{6}{\pi}\tan^{-1}\left(\frac{h}{\sqrt{2d^2+h^2}}\right)\right]y$$

$$= 0.$$

Solving for y as a function of x it is therefore required that

$$y = \frac{x}{\dfrac{6}{\pi}\tan^{-1}\left(\dfrac{h}{\sqrt{2d^2+h^2}}\right)},$$

in order to obtain $\varepsilon_{ax}=0$ at the center of a dot of finite height.

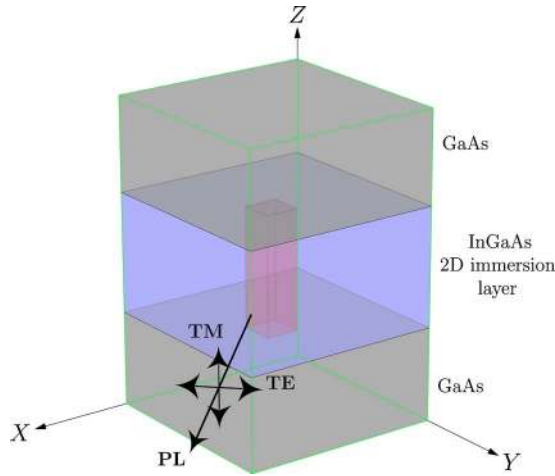Figure 1 shows, as a function of the aspect ratio h/d, the

FIG. 2. (Color online) Schematic image of an InGaAs CQD in center of image (red) with InGaAs 2D surrounding (immersion) layer in the plane (blue) and GaAs host material above and below (gray). The arrows show the direction of the considered in-plane emission and the respective linear light polarization directions (TE and TM).

FIG. 3. (Color online) Total (red empty bars) and the z (TM) component (blue filled bars) of the transition oscillator strength (left axis) of a cuboidal QD with aspect ratio equal to 3 and with QD In content equal to 45% for three different In contents in the 2D surrounding layer. The full green squares joined by lines show the light hole contribution to the total valence wave function (right axis).

value of the contrast ratio $(y+x)/x$ required in order to achieve zero net strain at the center of a columnar In$_{x+y}$Ga$_{1-x-y}$As dot embedded in an In$_x$Ga$_{1-x}$As QW between GaAs barriers. It can be seen that the contrast ratio approaches three with increasing aspect ratio, implying that the TM and TE polarization intensities should be approximately equal in an infinitely high QD when the In composition in the dot is three times that in the well. For reasonably realistic aspect ratios ($h/d \approx 3-6$), we estimate that the In content in the QD should be approximately four times larger than that in the QW in order to get equal intensity TE and TM emission.

B. Numerical simulations

The geometrical model of the columnar QD with 2D surrounding (immersion) layer is presented in Fig. 2, including an illustration of the linear polarization directions. The TE-mode polarization vector lies in the x-y plane, while the TM-mode is polarized along the growth (z) direction. Light is considered to be emitted from the CQD along either the [110] or [1$\bar{1}$0] direction. The CQD is placed in the center of the box and the height of the 2D immersion layer is assumed the same as the height of the CQD (see the transmission electron microscopy images in Refs. 17, 19, and 44). All the simulations presented assume a cuboid QD with a square base of diagonal length 20 nm (14.14 nm base length), and with the aspect ratio (height to base length) changed from 3 to 6 (height between 42.42 and 84.84 nm). All the material parameters used in the calculations are taken from Ref. 45, assuming room temperature values for the lattice constants and energy band gaps. We use a larger numerical box for the calculation of the strain field than for the energy levels. For the former, the box has a border of 45 nm width and a mesh length of 4 Å, whereas for the latter the box border is 15 nm wide and the mesh length 5 Å. In all cases, fourteen conduction band energy levels are calculated and forty valence band levels. The assumed geometry and the material compositions
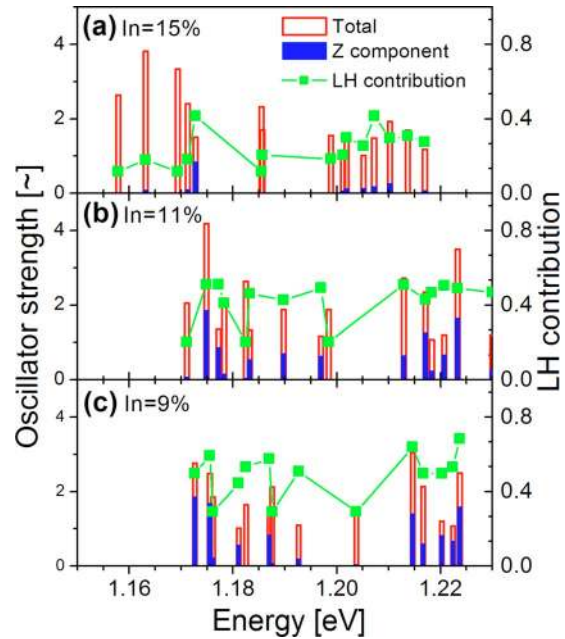
are taken in the ranges around the experimentally determined values, focusing on values which are promising from the point of view of polarization independent emission in GaAs-based CQD structures.[18,19,44]

Figure 3 shows the calculated total intensities of the optical transitions and the fraction of the intensity in the TM polarization for a CQD with an aspect ratio of 3 and In content of 45% inside the dot. The In content in the immersion layer is changed from 15% down to 9% in Figs. 3(a)–3(c), respectively, (which corresponds to the compositional contrast between the dot and the 2D surrounding changing from 3 to 5). For clarity, only those transitions which have a significant intensity are shown. In addition, we also plot on the right hand axes in Fig. 3 the LH contribution to each valence band wave function, where the EL, HH, LH, and SO components (C_{EL}, C_{HH}, C_{LH}, and C_{SO}, respectively) $\vec{\phi}=[\phi^1_{EL}, \phi^2_{EL}, \phi^1_{LH}, \phi^1_{HH}, \phi^2_{HH}, \phi^2_{LH}, \phi^1_{SO}, \phi^2_{SO}]$ have been calculated as[16]

$$C_M = \int_V \sum_{j=1}^{2} |\phi^j_M|^2 d^3\vec{r}.$$

Both the electron and SO components typically contribute of the order of 1%–2% or less to the overall probability density of the different valence band states. Therefore, they are neglected in the further discussion because the linear polarization selection rules (and hence the TE-mode and TM-mode intensities) are then determined primarily by the contributions from the HH and LH states only.

Several conclusions can be drawn directly from Fig. 3. We see that there is a significant TM polarization contribution when both the aspect ratio and the content contrast
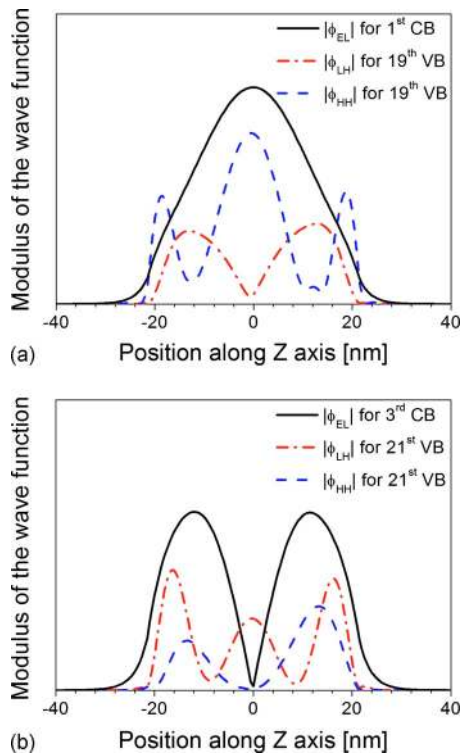
FIG. 4. (Color online) The cross-sections along the *z*-axis through the middle of the QD of the modulus of the 3D wave functions for a cuboid with aspect ratio 3 and with In content equal to 45% in the QD and to 9% in the surrounding layer. (a) the EL components (solid black line) of the 1st conduction wave function and the LH (dash dot red line), and HH (dashed red line) components of the 19th valence wave function and (b) the EL components (solid black line) of the 3rd conduction wave function and the LH (dash dot red line) and HH (dashed blue line) components of the 21st valence wave function.

equals 3 [Fig. 3(a)] but this contribution is mainly found in the higher order transitions, and so TM will definitely not dominate over TE recombination in the full (i.e., integrated intensity) spectrum. Decreasing the In content in the surrounding layer causes a significant increase in the TM component of the lowest energy transitions [Figs. 3(b) and 3(c)]. In most cases the enhanced TM intensity is correlated with an increased LH contribution to the valence wave function (see the right axis in Fig. 3) but transitions with a LH contribution of about 50% and with corresponding very small TM component are also present. Such transitions can be found in Fig. 3(b) at energy around 1.178, 1.213, and 1.218 eV, and in Fig. 3(c) at 1.183, 1.193, and 1.217 eV. For Fig. 3(a), there are transitions at 1.186 and 1.199 eV with LH contribution about 20% but again with very small TM component. In order to explain these cases we will discuss the wave function properties for one example in more detail.

Figure 4 shows the calculated modulus of the different components of two conduction and two valence band wave functions, plotted along the *z*-axis through the center of a cuboid with aspect ratio 3 and with In content equal to 45% and 9% in the QD and immersion layer, respectively. Figure 4(a) shows the LH and HH components, $|\phi_{LH}|$ and $|\phi_{HH}|$ of the 19th valence band wave function which, with the first conduction wave function, corresponds to the transition at 1.178 eV in Fig. 3(c). It is seen that there is a dip in $|\phi_{LH}|$ in

the middle of the QD, suggesting that this is an odd function along the *z*-axis, whereas $|\phi_{HH}|$ is clearly an even function. The first conduction function is also even along the *z*-axis. As a result it has a significant overlap with the HH component but despite a large LH contribution to the valence wave function the TM related intensity remains negligible. Figure 4(b) shows the electron component of the third conduction band state for the CQD of Fig. 3(b). This wave function, together with the 21st valence band function (also presented in the same figure), gives the transition at 1.193 eV. It can be seen that the LH part is an even function whereas the HH part is predominantly an odd function along the *z*-axis. Because the EL contribution to the third conduction wave function is odd, we have again a similar situation to the previously discussed transition.

Hence, we conclude that there can be a large LH contribution to a valence state but due to the symmetry properties of the components of the initial and final states, some transitions involving this state can still have a very small TM related polarization intensity. This property is independent both of the In content in the QD or 2D immersion layer and also of the aspect ratio. Figure 4 shows that there is not always a direct connection between the contribution of LHs to a valence states and the TM intensity of a given transition.

In order to allow for a more direct comparison with experimental data on an ensemble of dots, the calculated transitions from Fig. 3 have been broadened by Gaussians with standard deviation equal to 20 meV. This imitates the inhomogeneous broadening in real structures, which is mainly related to the nonuniformity of the dot properties within the ensemble. As the experiments are usually performed at room temperature (as indeed needed in applications), we simulate the effects of temperature by introducing the Boltzmann function (for 300 K), which imitates the temperature dependent carrier distribution over the conduction and valence band states, and makes the calculated results easier to compare with emission spectra from photoluminescence or electroluminescence. The calculated Gaussian broadened room temperature spectra are shown in Fig. 5 for both the TE and TM intensity components. It can be seen that the TM intensity approaches the TE one for the highest In contrast ratio. Because of the carrier distribution effect, the stronger TM intensity associated with higher energy transitions in Fig. 3 is less notable in the more realistic emissionlike spectra of Fig. 5. With decreasing In content in the immersion layer (increasing content contrast) the TM related intensity becomes stronger and the effective TE peak position shifts to higher energy while the TM one shifts to lower energy, giving almost equal TM and TE intensities in the low energy part of the spectrum for a content contrast of 5 [Fig. 5(c)].

For further analysis we integrated the TM and TE spectral functions (as those in Fig. 5) and calculated the TM to TE total intensity ratio for several structures. The solid lines in Fig. 6 show the calculated intensity ratio as a function of the aspect ratio for different composition contrasts (obtained by changing the 2D immersion layer In content from 15% to 11% and 9%). It can be seen (red line, squares), that if the difference in the In content between the dot and the surrounding is too low (45% and 15% in the QD and immersion
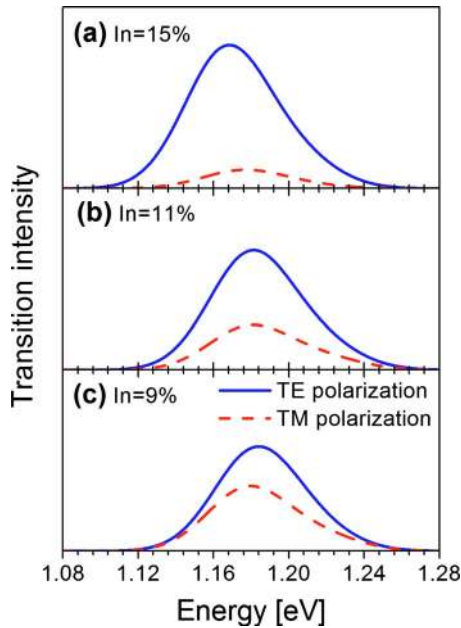
FIG. 5. (Color online) TE (solid blue) and TM (dashed red) intensities for a QD with In content of 45%, aspect ratio equal to 3 and different immersion layer In contents. The transition energies are broadened by a Gaussian function with standard deviation equal to 20 meV. The Boltzman distribution function has been applied to simulate the carrier distribution at room temperature.

layer, respectively), then changing the aspect ratio will not affect the TM and TE intensities significantly, and it will not be possible to achieve polarization insensitivity. This result qualitatively explains the experimental results reported in Ref. 14. On the other hand, when the content contrast ratio is high enough (45% to 9%) it enhances the intensity for TM polarization for even relatively low dot heights and, the larger the composition contrast, the stronger the influence of the aspect ratio of the dot. For an aspect ratio between 5 and 6 (and contents 45% to 9%), the TM to TE intensity ratio reaches 1. The dashed lines show the value of the biaxial strain in the middle of the CQD (numerically calculated), which is included for comparison with the analysis made in Sec. III A. It can be seen that the computed results agree with the general conclusions of the analytical model. For instance, the decrease in the biaxial strain with increasing dot height is
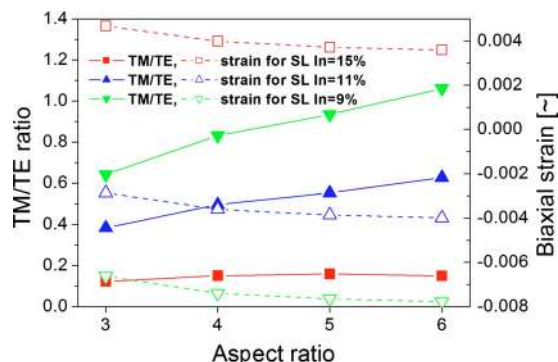

FIG. 6. (Color online) Calculated TM to TE polarization total intensity ratio at room temperature (solid lines) for a QD In content of 45% and for various In contents in the 2D surrounding layer vs the dot aspect ratio. The dashed lines show the value of the biaxial strain in the middle of the CQD.
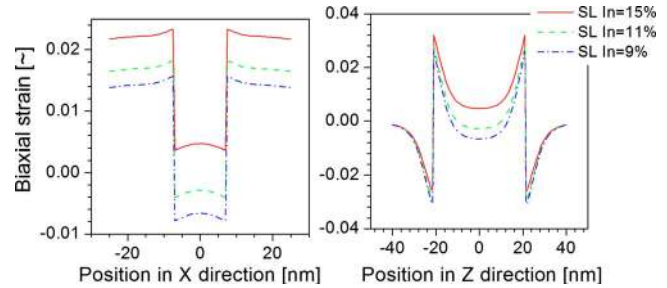

FIG. 7. (Color online) Biaxial strain distribution along the *x* and *z* axes through the center of the QD with In content of 45% and with aspect ratio equal to 3 for various In contents in the surrounding layer.

correlated with the increase in the TM to TE ratio. Further, compressive strain (positive values) in the middle of the dot always leads to TE domination and, the more tensile the strain becomes (with increasing In contrast ratio between the dot and the surrounding immersion layer), the stronger becomes the TM component in the transition intensity. However, there are some details of these dependences, which could not be calculated within the model in the Sec. III A. The numerically calculated biaxial strain in the middle of the dot does not change much with aspect ratio, e.g., the strain changes only by approximately 0.001 for the content contrast 5 as the aspect ratio increases from 3 to 6 (see the green dashed line in Fig. 6), whereas the TM/TE ratio changes from approximately 0.7 to 1.3. Also the change in the biaxial strain is approximately the same for each considered content ratio while the polarization ratio becomes stronger for higher compositional contrast. Moreover, as we discussed qualitatively in Sec. III A, full compensation of the biaxial strain in the middle of the dot will probably not be enough, and some overcompensation (tensile strain) will be necessary to favor the LH contribution. Here, the numerical results give the quantitative measure. They show for the examples considered here that the TM and TE integrated intensities become equal for a tensile strain on the level of 0.0075 in the middle of the dot.

In order to understand the reasons for the behavior observed in Fig. 6, we plot the calculated biaxial strain distribution values through the center of the CQD along the growth direction, i.e., *z*-axis, and along an in-plane direction, i.e., *x*-axis, for a fixed aspect ratio of 3 and different composition contrasts in Fig. 7, and for a fixed content ratio of about 4 and different aspect ratios in Fig. 8. Both these figures show already a coincidence between the results on the TM and TE intensities and the strain distribution. However, it is not so direct because there are areas inside the dot where the biaxial strain can change sign. In general, the more negative is the biaxial strain and the larger the fraction of the dot for which it is negative (especially near the dot center) then the stronger the TM intensity will be. This is understandable because the increased tensile character leads to a greater LH contribution to the valence wave functions inside the dot. In order to have a better insight into the relationship between strain and polarization, we introduce a new figure of merit, defined as the integral of the biaxial strain function over the QD volume (in 3D). Because this value measures the strain

over the entire QD and not only at a single position, it thus gives a more appropriate indication of the overall strain state.

Figure 9 compares the simple biaxial strain at the center of the CQD with the integrated biaxial strain over the QD for In content equal to 45% and for various In contents in the immersion layer. For In content contrast equal to 4 and 5, an increase in the aspect ratio causes a decrease both of the biaxial strain and of the integrated biaxial strain (the decrease in the latter is much stronger) while for In contrast equal to 3 an increase in the aspect ratio causes a decrease in the biaxial strain at the center, but an increase in the integrated biaxial strain. This behavior is found for all cases which we have investigated. For other In contents in the QD (60% and 75%) and In content contrast equal to 3 the simple and integrated biaxial strain have opposite dependences on the aspect ratio. For In contrast equal to 4 and 5, both strain values decrease with increasing aspect ratio. The importance of the integrated biaxial strain can be explained in the following way. The carrier wave function samples a large fraction of the total volume of the QD rather than just one particular point in the QD. Therefore, the total strain affects the electronic states rather than its value at just one point, and hence correlates better with the overall TM/TE behavior. Moreover, the variation in the biaxial strain with aspect ratio is approximately the same in the dot center regardless of the In contrast ratio, whereas the slope of the TM/TE intensities ratio dependence is much more sensitive to the content contrast and aspect ratio, and is therefore, much better described by the integrated biaxial strain function.

Figure 10 shows, as a function of aspect ratio, the integrated TM to TE intensity ratio for different In contents in the QD (45%, 60%, and 75%) and for the composition contrast in the range of 3–5. Based on that and the previous discussion, the necessary condition for getting polarization independent emission from a CQD (efficient TM intensity) can be drawn, the integrated biaxial strain over the QD needs to be negative—the strain value in the dot center can then be treated as a first approximate requirement. The behavior of the TM/TE ratio depends primarily on the In composition ratio, and is rather independent of In composition in the QD itself. Figure 10 shows also what are the conditions for obtaining equal TM and TE intensity. For a composition contrast close to 5, polarization independent recombination can be obtained for moderate aspect ratios of around 4, as already demonstrated experimentally.[19] When the contrast ratio

is closer to 4, a very high aspect ratio ($>$6) is then required. Additionally, for composition contrasts of three and below tuning the aspect ratio will not help to make the TM intensity of the transitions comparable to the TE related ones.

There are some details which are not seen directly in Fig. 10. Figure 11 shows the normalized transition intensities in both polarizations for contrast ratio equal to 5, for various In contents in the QD and aspect ratios of 5 or 6, i.e., for parameters which are in the range to give almost equal total TM and TE intensities. However, as can be seen, this does not necessarily mean that both spectral response functions are identical. Usually, as was already seen in Fig. 5, the TE and TM lineshapes are slightly different and the peak positions can be shifted by several milli-electron-volt. From the application point of view, where we aim for equal gain in both polarizations over a broad wavelength range, it would

FIG. 9. (Color online) Biaxial strain (solid line) in the middle of the QD and integrated biaxial strain (dashed line) over the QD for an In content in the QD equal to 45% and various In content in 2D surrounding layer, plotted as a function of QD aspect ratio.
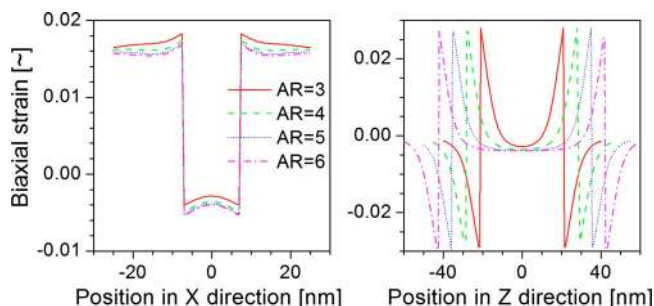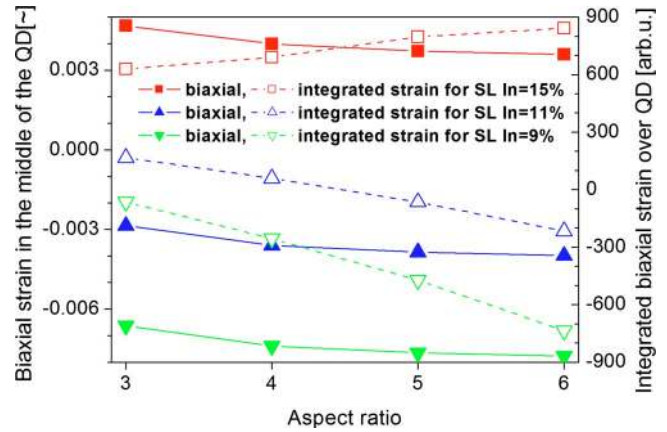

FIG. 8. (Color online) Biaxial strain distribution along the *x* and *z* axes for the QD with In content of 45% and with In content of 11% in the surrounding layer, for various aspect ratio values.
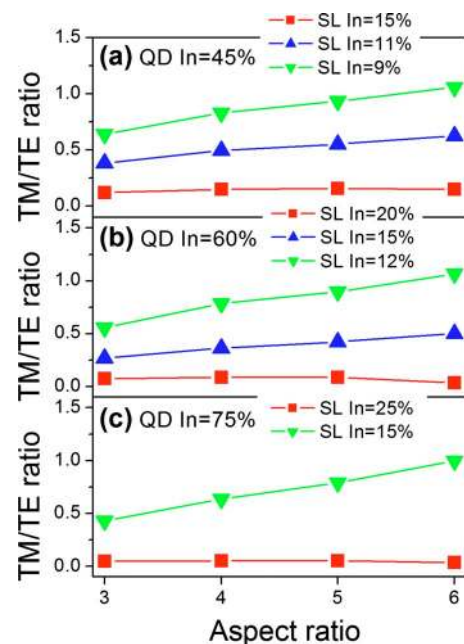

FIG. 10. (Color online) TM/TE intensity ratio (at room temperature) for QD In content 45%, 60%, and 75%, and content contrast ratio between 3 and 6 as a function of the dot aspect ratio.
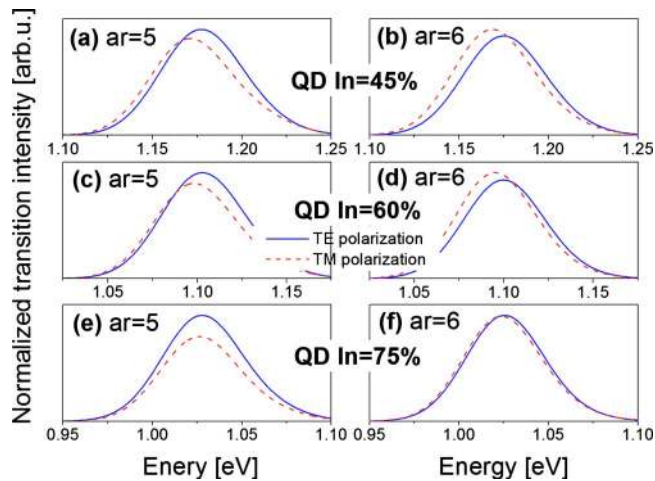
FIG. 11. (Color online) Normalized intensity of TE (solid blue) and TM (dashed red) transitions for various QDs with contrast ratio equal to 5, [(a) and (b)] for QD In content of 45% with aspect ratio, ar=5 and 6, respectively, [(c) and (d)] for QD In content of 60% with ar=5 and 6, respectively, and [(e) and (f)] for QD In content of 75% with ar=5 and 6, respectively.

be optimal to avoid these differences. This can be achieved by two approaches. The first of these requires precise structure engineering and proper choice of aspect ratio and In contents, as in Fig. 11(f), where there the QD has 75% In content, aspect ratio of 6 and a composition contrast of 5 with the surrounding 2D immersion layer. Second, it should be possible to use postgrowth fine tuning of actual device structures for instance by postgrowth annealing or application of an electrical bias. Either of these could modify the TM and TE intensities for each transition, and hence affect the effective peak shapes and their relative energy positions.

The theoretical results presented here are in good qualitative agreement with the available but still limited experimental data on InGaAs/GaAs CQDs, including the dependence both on aspect ratio and on composition contrast,[14] showing the practical applicability of our modeling. It has for instance been observed that increasing the aspect ratio, for an approximately constant composition contrast, can cause a significant enhancement of the TM polarization intensity in the edge-emitted electroluminescence. The absolute values of TM to TE intensity ratio are actually higher in the experiment compared to our theoretical predictions. This could be due to additional factors, which can occur in the real structures but which were not included in the calculations, such as composition inhomogeneities and gradients in the vertical (growth) direction within both the dot and the immersion layer. For instance, effects as indium segregation between the higher content columnar dot and lower content immersion layer can cause an effective increase in the composition contrast due to depleting with indium atoms the nearest neighborhood of the dot and hence enhance the TM to TE ratio.

IV. CONCLUSIONS

We have theoretically studied the optical properties of $In_zGa_{1-z}As/GaAs$ CQDs from the point of view of their possible application in polarization independent optical amplifiers. We have taken into consideration and shown the impor-

tance of a 2D $In_xGa_{1-x}As$ layer of lower composition ($x < z$), which surrounds such dots in-plane in real structures. We have shown how this immersion layer strongly affects the linear polarization properties and controls the selection rules for optical transitions in such dots for light propagation in the growth plane. We have shown not only how important is the composition contrast z/x between the dot material and this 2D layer, but also given the necessary condition to obtain full polarization independence in the emission spectrum. This requires that the biaxial strain integrated over the CQD volume has a negative value. We find that the value of the integrated biaxial strain correlates well with the dependence of the TM/TE intensity ratio on dot aspect ratio and on compositional contrast. We have shown that for an aspect ratio equal to 5 and for an In composition contrast equal to 5 it is possible to obtain efficient TM emission from a CQD, regardless of the In content in the QD. Conditions for achieving equal TE and TM intensities have been found, confirming the potential value of CQDs for use in polarization insensitive semiconductor optical amplifiers.

[1]M. Tadić, F. M. Peeters, and K. L. Janssens, Phys. Rev. B **65**, 165333 (2002).
[2]M. Grundmann, O. Stier, and D. Bimberg, Phys. Rev. B **52**, 11969 (1995).
[3]C. E. Pryor and M. E. Pistol, Phys. Rev. B **72**, 205311 (2005).
[4]W. Lee, J.-M. Myoung, Y.-H. Yoo, and H. Shin, Solid State Commun. **132**, 135 (2004).
[5]M. A. Cusack, P. R. Briddon, and M. Jaros, Phys. Rev. B **56**, 4047 (1997).
[6]C. Pryor, Phys. Rev. B **60**, 2869 (1999).
[7]S. I. Rybchenko, G. Yeap, R. Gupta, I. E. Itskevich, and S. K. Haywood, J. Appl. Phys. **102**, 013706 (2007).
[8]O. Stier, M. Grundmann, and D. Bimberg, Phys. Rev. B **59**, 5688 (1999).
[9]K. Kawaguchi, N. Yasuoka, M. Ekawa, H. Ebe, T. Akiyama, M. Sugawara, and Y. Arakawa, Appl. Phys. Lett. **93**, 121908 (2008).
[10]K. Kawaguchi, N. Yasuoka, M. Ekawa, H. Ebe, T. Akiyama, M. Sugawara, and Y. Arakawa, Jpn. J. Appl. Phys., Part 2 **45**, L1244 (2006).
[11]T. Kita, N. Tamura, O. Wada, M. Sugawara, Y. Nakata, H. Ebe, and Y. Arakawa, Appl. Phys. Lett. **88**, 211106 (2006).
[12]N. Yasuoka, K. Kawaguchi, H. Ebe, T. Akiyama, M. Ekawa, S. Tanaka, K. Morito, A. Uetake, M. Sugawara, and Y. Arakawa, Appl. Phys. Lett. **92**, 101108 (2008).
[13]P. Podemski, G. Sek, K. Ryczko, J. Misiewicz, S. Hein, S. Höfling, A. Forchel, and G. Patriarche, Appl. Phys. Lett. **93**, 171910 (2008).
[14]P. Ridha, L. Li, A. Fiore, G. Patriarche, M. Mexis, and P. M. Smowton, Appl. Phys. Lett. **91**, 191123 (2007).
[15]K. Mukai, Y. Nakata, H. Shoji, M. Sugawara, K. Ohtsubo, N. Yokoyama, and H. Ishikawa, Electron. Lett. **34**, 1588 (1998).
[16]T. Saito, H. Ebe, Y. Arakawa, T. Kakitsuka, and M. Sugawara, Phys. Rev. B **77**, 195318 (2008).
[17]L. H. Li, G. Patriarche, N. Chauvin, P. Ridha, M. Rossetti, J. Andrzejewski, G. Sek, J. Misiewicz, and A. Fiore, IEEE J. Sel. Top. Quantum Elec-

tron. **14**, 1204 (2008).

[18] L. H. Li, G. Patriarche, M. Rossetti, and A. Fiore, J. Appl. Phys. **102**, 033502 (2007).

[19] L. H. Li, G. Patriarche, and A. Fiore, J. Appl. Phys. **104**, 113522 (2008).

[20] O. Stier and D. Bimberg, Phys. Rev. B **55**, 7726 (1997).

[21] A. Schliwa, M. Winkelnkemper, and D. Bimberg, Phys. Rev. B **76**, 205324 (2007).

[22] C. Pryor, M. E. Pistol, and L. Samuelson, Phys. Rev. B **56**, 10404 (1997).

[23] C. Pryor, J. Kim, L. W. Wang, A. J. Williamson, and A. Zunger, J. Appl. Phys. **83**, 2548 (1998).

[24] I. P. Ipatova, V. G. Malyshkin, and V. A. Shchukin, J. Appl. Phys. **74**, 7198 (1993).

[25] B. Jogai, J. Appl. Phys. **88**, 5050 (2000).

[26] G. Bester, X. F. Wu, D. Vanderbilt, and A. Zunger, Phys. Rev. Lett. **96**, 187602 (2006).

[27] T. L. Li and K. J. Kuhn, J. Comput. Phys. **110**, 292 (1994).

[28] T. B. Bahder, Phys. Rev. B **41**, 11992 (1990); **46**, 9913(E) (1992).

[29] W. Sheng and J.-P. Leburton, Phys. Rev. B **64**, 153302 (2001).

[30] K. Boujdaria, S. Ridene, and G. Fishman, Phys. Rev. B **63**, 235302 (2001).

[31] T. Ando and H. Akera, Phys. Rev. B **40**, 11619 (1989).

[32] B. Laikhtman, Phys. Rev. B **46**, 4769 (1992).

[33] G. T. Einevoll and L. J. Sham, Phys. Rev. B **49**, 10533 (1994).

[34] M. J. Godfrey and A. M. Malik, Phys. Rev. B **53**, 16504 (1996).

[35] A. V. Rodina, A. Y. Alekseev, A. L. Efros, M. Rosen, and B. K. Meyer, Phys. Rev. B **65**, 125302 (2002).

[36] I. V. Tokatly, A. G. Tsibizov, and A. A. Gorbatsevich, Phys. Rev. B **65**, 165328 (2002).

[37] M. E. Pistol, J. Phys. Soc. Jpn. **71**, 1325 (2002).

[38] G. A. Baraff and D. Gershoni, Phys. Rev. B **43**, 4011 (1991).

[39] W. Shyy, J. Comput. Phys. **57**, 415 (1985).

[40] G. L. G. Sleijpen and H. A. Van der Vorst, SIAM J. Matrix Anal. Appl. **17**, 401 (1996).

[41] R. G. Veprek, S. Steiger, and B. Witzigmann, Phys. Rev. B **76**, 165320 (2007).

[42] F. Szmulowicz, Phys. Rev. B **51**, 1613 (1995).

[43] J. R. Downes, D. A. Faux, and E. P. O'Reilly, J. Appl. Phys. **81**, 6700 (1997).

[44] L. H. Li, P. Ridha, G. Patriarche, N. Chauvin, and A. Fiore, Appl. Phys. Lett. **92**, 121102 (2008).

[45] I. Vurgaftman, J. R. Meyer, and L. R. Ram-Mohan, J. Appl. Phys. **89**, 5815 (2001).